

Quantitatively predicting angle-resolved polarized Raman intensity of black phosphorus flakes

Tao Liu^{1,2,‡}, Jia-Liang Xie^{1,2,‡}, Yu-Chen Leng¹, Rui Mei^{1,2}, Heng Wu^{1,2}, Jiahong Wang³, Yang Li³, Xue-Feng Yu³, Miao-Ling Lin^{1,2,*} and Ping-Heng Tan^{1,2,†}

¹ State Key Laboratory of Superlattices and Microstructures,
Institute of Semiconductors, Chinese Academy of Sciences, Beijing 100083, China

² Center of Materials Science and Optoelectronics Engineering,

University of Chinese Academy of Sciences, Beijing, 100049, China

³ Shenzhen Engineering Center for the Fabrication of Two-Dimensional Atomic Crystals,
Shenzhen Institutes of Advanced Technology, Chinese Academy of Sciences, Shenzhen 518055, China and

[‡] Contributed equally to this work

In this study, we propose two strategies to determine complex refractive indexes along armchair and zigzag axes for BP flakes, aiming in predicting angle-resolved polarized Raman (ARPR) intensity by explicitly considering birefringence, linear dichroism, and anisotropic cavity interference effects within multilayered structures. By leveraging this methodology, we have identified the intrinsic complex Raman tensors for phonon modes of BP flakes, independent of BP flake thickness (>20 nm). We also elucidated the flake thickness-dependent effective complex Raman tensor elements, allowing for precise prediction of the observed ARPR intensity profile for specific BP flake. This framework can be extended to other ALM flakes deposited on dielectric substrate to determine the Raman tensors for fully predicting their ARPR response.

Raman scattering intensity depends on the direction of incident laser and collected Raman light relative to the principal axes of the crystal[1, 2], whose polarization vectors are \mathbf{e}_i and \mathbf{e}_s , respectively. The Raman tensor \mathbf{R} serves as a crucial component in determining the Raman intensity by $I \propto |\mathbf{e}_s^T \cdot \mathbf{R} \cdot \mathbf{e}_i|^2$ (Fig.1(a1))[1]. By altering the direction of \mathbf{e}_i and \mathbf{e}_s with respect to the crystallographic axes, angle-resolved polarized Raman (ARPR) intensity can be estimated[1, 3–6]. In most cases, only real Raman tensor is generally involved in calculating ARPR intensity for bulk crystals[3–5]. However, in H.B. Ribeiro’s pioneering work[6], the unusual ARPR spectra in black phosphorus (BP) flakes (360nm thickness) can be explained only by considering complex Raman tensor, inspiring huge efforts to understand the corresponding results after taking birefringence and linear dichroism effects into account in detail[5–18]. The fitted \mathbf{R} (amplitude ratio and phase difference between two tensor elements) were sensitive to the flake thickness and the layer thickness of substrate dielectrics[6–14], making it impossible to predict ARPR spectrum for BP flakes with different thickness and on different substrates.

In principle, Raman tensor is an inherent parameter for a crystal to understand its Raman spectrum [1, 3, 19], regardless of its volume[20], dimensionality[21, 22] and even its counterpart[20, 23] in multilayer dielectrics. For anisotropic layered materials (ALMs), such as BP, the birefringence and linear dichroism effects result in depth (y)-dependent polarization and amplitude of both excitation and scattered electric fields at the

location of the scattering event[5]. Thus, the y -dependent polarization vectors $\mathbf{e}'_s(y)$ and $\mathbf{e}'_i(y)$ [5] cannot be treated as constants of \mathbf{e}_s and \mathbf{e}_i (Fig.1(a2))[5, 24–27], respectively. Therefore, it is crucial to unveil the intrinsic Raman tensor \mathbf{R}_{int} correlated with $\mathbf{e}'_s(y)$ and $\mathbf{e}'_i(y)$ to estimate Raman intensity at depth y within BP flakes by $I(y) \propto |\mathbf{e}'_s{}^T(y) \cdot \mathbf{R}_{\text{int}} \cdot \mathbf{e}'_i(y)|^2$. Flake-substrate multilayer dielectrics can further modulate the light propagation within BP flakes due to the interference effects of excitation/scattered light[20, 28]. How to extract \mathbf{R}_{int} to quantitatively predict the ARPR response of BP flakes is thus a major challenge in this field.

In this letter, to quantitatively reproduce ARPR intensity profile of specific BP flakes on various SiO_2/Si substrate, we have extracted \mathbf{R}_{int} of BP by analyzing ARPR intensity profiles of BP flakes with different thickness (d_{BP}) or of specific BP flake deposited on SiO_2/Si substrate with different SiO_2 layer thickness (d_{SiO_2}). The light propagation within a BP flake modulated from birefringence, linear dichroism and interference effects in air/BP/ SiO_2/Si multilayers are fully taken into account. Contour plots of effective Raman tensor elements as functions of d_{BP} and d_{SiO_2} are generated to quantitatively predict ARPR intensity of specific BP flakes on any substrates without fitting parameters. This work provides a comprehensive insight into anisotropy and Raman scattering in ALM flakes.

BP flakes were mechanically exfoliated onto SiO_2/Si substrates with varied d_{SiO_2} . Figure 1(b) shows the optical image of BP flakes with $d_{\text{BP}} \sim 139\text{nm}$, as measured by atomic force microscopy (AFM). BP is a van der Waals semiconductor with strong in-plane anisotropy along the zigzag(ZZ) and armchair(AC) axes, belonging to the orthorhombic symmetry (i.e., D_{2h} symmetry). We establish the X and Z axes in alignment with the ZZ

* linmiaoling@semi.ac.cn

† phtan@semi.ac.cn

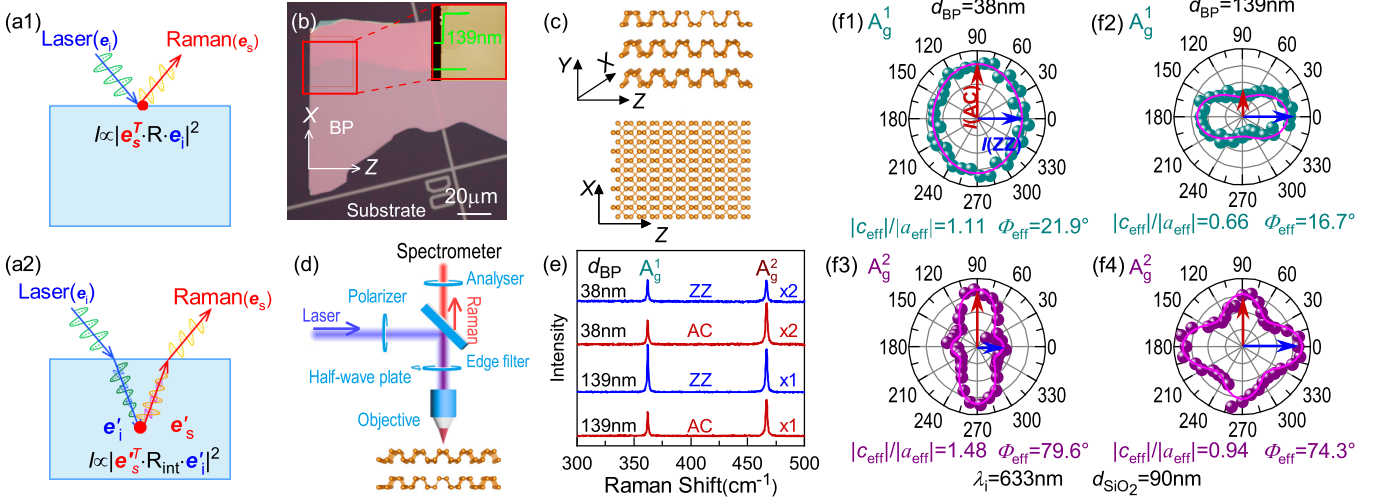


FIG. 1. Schematic diagram of Raman scattering event (a1) expressed by Raman tensor \mathbf{R} and that (a2) within ALM governed by \mathbf{R}_{int} , oblique incidence for convenience. (b) Optical image of BP flake with $d_{BP}=139\text{nm}$ measured by AFM (inset). (c) Crystallographic structure of BP from the side and top views. (d) Schematic diagram of ARPR spectroscopy setup. (e) Raman spectra of BP flakes with $d_{BP}=38\text{nm}$ and 139nm on $90\text{nm-SiO}_2/\text{Si}$ substrate, and (f) the corresponding ARPR intensity profiles of the A_g^1 and A_g^2 modes excited by $\lambda_i=633\text{nm}$, and the fitted $|c_{eff}|/|a_{eff}|$ and Φ_{eff} are indicated.

and AC directions[5], respectively (Fig.1(c)). We utilized the Raman setup in Fig.1(d) to measure the ARPR response of BP flakes at normal laser incidence on the basal plane under a parallel polarization configuration. The \mathbf{e}_i and \mathbf{e}_s relative to the ZZ axis (θ) are controlled by the half-wave plate in the common optical path to measure ARPR intensity of BP flakes, with $\theta = 0^\circ$ for $\mathbf{e}_i(\mathbf{e}_s) \parallel \text{ZZ}$ axis and $\theta = 90^\circ$ for $\mathbf{e}_i(\mathbf{e}_s) \parallel \text{AC}$ axis. In this case, $\mathbf{e}_i=\mathbf{e}_s=(\cos\theta, 0, \sin\theta)^T$. Figure 1(e) plots the Raman spectra of BP flakes with $d_{BP}=38\text{nm}$ and 139nm for $\mathbf{e}_i(\mathbf{e}_s) \parallel \text{ZZ}$ and $\mathbf{e}_i(\mathbf{e}_s) \parallel \text{AC}$, where two typical Raman modes, i.e., A_g^1 and A_g^2 modes are observed at 362cm^{-1} and 466cm^{-1} , respectively. The Raman intensity ratio of A_g^1 (A_g^2) mode between $\mathbf{e}_i(\mathbf{e}_s) \parallel \text{ZZ}$ ($I(\text{ZZ})$) and $\mathbf{e}_i(\mathbf{e}_s) \parallel \text{AC}$ ($I(\text{AC})$) varied with d_{BP} , as depicted in the ARPR intensity (Fig.1(f)). The nonzero tensor elements R_{uv} for A_g mode are $R_{xx} = a$, $R_{yy} = b$, $R_{zz} = c$. Due to the normal incidence onto the basal plane, only a and c are involved. By utilizing \mathbf{R} with effective complex tensor elements, $a = |a_{eff}|e^{i\Phi_a}$ and $c = |c_{eff}|e^{i\Phi_c}$ ($\Phi_{eff}=\Phi_c - \Phi_a$)[6–9, 12, 14, 18], one can connect the experimentally measured ARPR intensity with \mathbf{e}_i and \mathbf{e}_s by $I \propto |\mathbf{e}_s^T \cdot \mathbf{R} \cdot \mathbf{e}_i|^2$, i.e.,

$$I \propto |a_{eff}|^2 \cos^4\theta + |c_{eff}|^2 \sin^4\theta + 2|a_{eff}||c_{eff}|\sin^2\theta \cos^2\theta \cos\Phi_{eff}. \quad (1)$$

By fitting the ARPR intensity with the Eq.1, $|c_{eff}|/|a_{eff}|$ and Φ_{eff} can be obtained. The fitted Φ_{eff} are different for A_g^1 and A_g^2 modes and vary with d_{BP} for each Raman mode. This contradicts the basic physical picture that Raman tensor is an inherent parameter for a crystal. Due to the in-plane anisotropy of BP flakes, the fitted $|c_{eff}|/|a_{eff}|$ and Φ_{eff} involve interplay

of various anisotropy effects (birefringence[8], linear dichroism effects[6] and anisotropic electron-photon (e-ph) and electron-phonon (e-phn) couplings[9]), distinct for different Raman modes and sensitive to d_{BP} , making it a challenge to predict the ARPR intensity of ALM flakes.

To tell apart various anisotropy effects on ARPR intensity of ALM flakes, as depicted in Fig.2(a1), the Raman scattering processes can be separated into the propagation paths of incident/scattered light and Raman scattering event at depth y . The latter is an inherent physical process governed by the anisotropic e-ph and e-phn couplings presented by \mathbf{R}_{int} , $I(y) \propto |\mathbf{e}_s^T(y) \cdot \mathbf{R}_{int} \cdot \mathbf{e}_i'(y)|^2$, in which $\mathbf{e}_s'(y)$ and $\mathbf{e}_i'(y)$ are modulated by birefringence and linear dichroism effects[5]. In addition, BP flakes commonly deposited onto SiO_2/Si substrate can generate a natural cavity due to the refractive index mismatch between BP flake and underlying substrate, where partial reflections of incident and scattered light occur at air/BP, BP/ SiO_2 and SiO_2/Si interfaces (Fig.2(a2) and Fig. S1). Thus, the modulus square of incident laser electric field in thick BP flakes does not decrease to zero even near BP/ SiO_2 interface (Fig. S2). Multiple reflection and optical interference can further modulate both $\mathbf{e}_s'(y)$ and $\mathbf{e}_i'(y)$. These modulations arising from birefringence, linear dichroism and optical interference effects shows evident in-plane anisotropy and can be described by the interference factor matrices of the incident laser ($J_i(y)$) and Raman signals ($J_s(y)$) at varied y using the transfer matrix method (TMM)[5, 20],

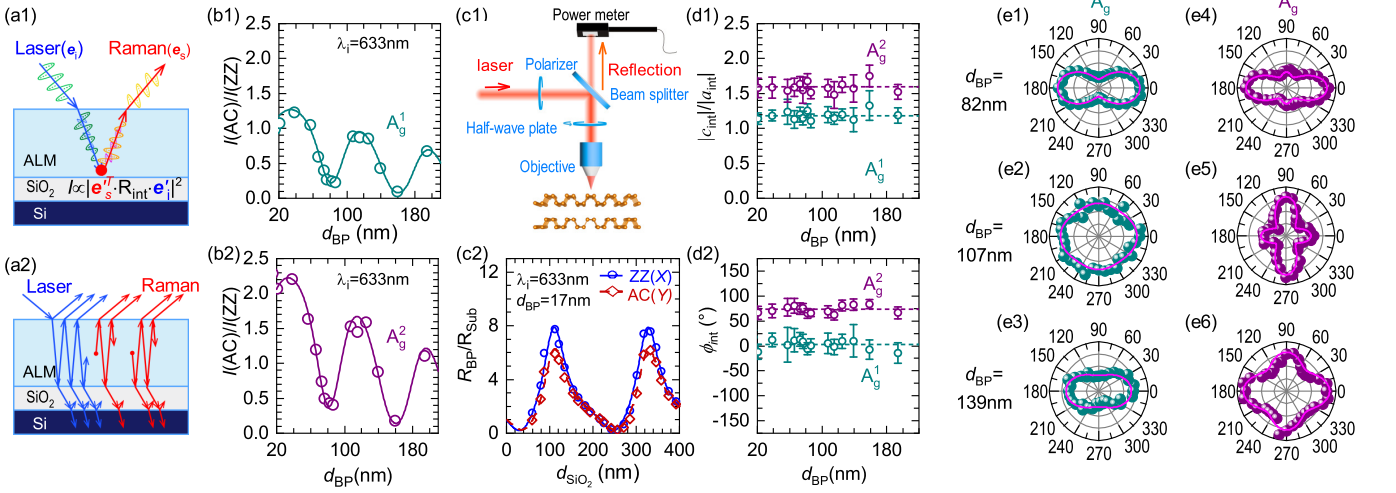


FIG. 2. Schematic diagrams (a1) for propagation paths of incident laser (blue) and scattered Raman signal (red) in ALM and (a2) for the interference effect of incident laser and scattered light within multilayer structure, oblique incidence for convenience. $I(AC)/I(ZZ)$ of (b1) A_g^1 and (b2) A_g^2 modes with $\lambda_i=633\text{nm}$. The solid lines are the fitted results. (c1) Schematic diagram of setup for reflectance measurement. (c2) Experimental (Symbols) and fitted (curves) reflectance of 17 nm BP flakes on SiO_2/Si substrates with varied d_{SiO_2} along AC and ZZ axes, which are normalized by that of bare SiO_2/Si substrates. (d1) $|c_{\text{int}}|/|a_{\text{int}}|$ and (d2) ϕ_{int} (open circles) and their averaged values (dashed lines) of A_g^1 and A_g^2 modes versus d_{BP} . (e) Experimental (filled circles) and calculated (pink lines) ARPR intensity profiles of A_g^1 and A_g^2 modes in BP/90nm- SiO_2/Si with different d_{BP} .

$$J_{i(s)}(y) = \begin{pmatrix} F_{i(s)X}(y) & 0 & 0 \\ 0 & 0 & 0 \\ 0 & 0 & F_{i(s)Z}(y) \end{pmatrix}. \quad (2)$$

where $F_{i(s)X}(y)$ and $F_{i(s)Z}(y)$ are respectively defined as the enhancement factors for incident laser (scattered signal) along X and Z axes, calculated by the TMM. Birefringence, linear dichroism and anisotropic interference effects in BP flakes always coexist under above-bandgap excitation and are manifested in the different values of $F_{i(s)X}(y)$ and $F_{i(s)Z}(y)$ due to the varied complex refractive indexes along X (\tilde{n}_X) and Z (\tilde{n}_Z) axes. Thus, $e_i^T(y) = J_i(y)e_i$ and $e_s^T(y) = e_s^T J_s(y)$. As the Raman scattered signals at each position y of the BP flakes contributes to the whole Raman intensity due to the cavity effect, the measured Raman scattered intensity for a given phonon mode from BP flake is the integration of Raman signal over d_{BP} , expressed as follows,

$$I \propto \int_0^{d_{\text{BP}}} |e_s^T J_s(y) \cdot \mathbf{R}_{\text{int}} \cdot J_i(y)e_i|^2 dy. \quad (3)$$

We express the nonzero elements of \mathbf{R}_{int} for A_g modes of BP flakes as $R_{xx} = |a_{\text{int}}|e^{i\phi_a}$, $R_{zz} = |c_{\text{int}}|e^{i\phi_c}$ and $\phi_{\text{int}} = \phi_c - \phi_a$, then the Eq.3 becomes:

$$I \propto \int_0^{d_{\text{BP}}} |F_{iX}(y)F_{sX}(y)|a_{\text{int}}|^2 e^{i\phi_a} \cos^2\theta + |F_{iZ}(y)F_{sZ}(y)|c_{\text{int}}|^2 e^{i\phi_c} \sin^2\theta|^2 dy. \quad (4)$$

Accordingly, $I(ZZ) \propto \int_0^{d_{\text{BP}}} |F_{iX}(y)F_{sX}(y)|a_{\text{int}}|^2 dy$ ($\theta = 0^\circ$) and $I(AC) \propto \int_0^{d_{\text{BP}}} |F_{iZ}(y)F_{sZ}(y)|c_{\text{int}}|^2 dy$ ($\theta = 90^\circ$). By fitting $I(AC)/I(ZZ)$ versus d_{BP} , one can obtain \tilde{n}_X , \tilde{n}_Z and $|c_{\text{int}}|/|a_{\text{int}}|$ for BP flakes. We summarized $I(AC)/I(ZZ)$ with incident laser wavelength (λ_i) of 633nm as a function of d_{BP} for A_g^1 and A_g^2 modes in Fig.2(b). The fitting of $I(AC)/I(ZZ)$ for these two modes are processed independently. The fitted \tilde{n}_X (\tilde{n}_Z) for A_g^1 and A_g^2 modes are almost identical to each other, whose averaged values are summarized in Table S1. The \tilde{n}_X and \tilde{n}_Z are confirmed by fitting the reflectance measurements (Fig.2(c1), Fig.S3) along X and Z axes of BP flakes with varied d_{BP} on 90nm- SiO_2/Si substrate, as compared in Table S3.

Because the intrinsic band structures of thick BP flakes ($>20\text{nm}$) should resemble the bulk and thus their \tilde{n}_X and \tilde{n}_Z will be independent of the BP flake thickness. However, when BP flakes thin down to a few layers, the electronic properties are highly dependent on the number of layers and the \tilde{n}_X and \tilde{n}_Z will vary significantly with the thickness. Taking advantages of the sensitive reflectance of BP/ SiO_2/Si to d_{SiO_2} , \tilde{n}_X and \tilde{n}_Z for BP flake with specific thickness can also be fitted from the reflectance measurements of BP/ SiO_2/Si with varied d_{SiO_2} . As an example, by fitting the normalized reflectance of a 17nm BP flake deposited on SiO_2/Si substrates for 633nm laser in Fig.2(c2), its \tilde{n}_X and \tilde{n}_Z can be acquired (Table S4), which are comparable to the average values fitted from BP flakes with varied d_{BP} .

With the fitted average \tilde{n}_X and \tilde{n}_Z for BP flakes with varied d_{BP} , $F_{i(s)X}(y)$ and $F_{i(s)Z}(y)$ can be numerically calculated, and then $|c_{\text{int}}|/|a_{\text{int}}|$ and ϕ_{int} for the A_g^1 and

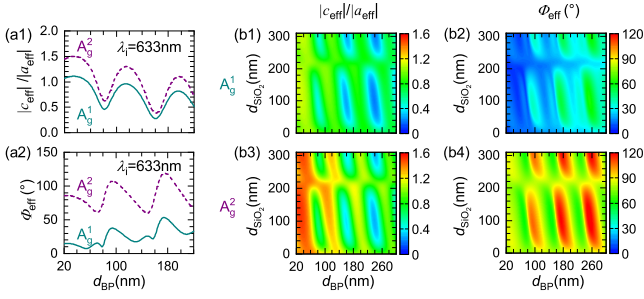


FIG. 3. Predicted (a1) $|c_{\text{eff}}|/|a_{\text{eff}}|$ and (a2) Φ_{eff} for A_g^1 and A_g^2 modes in BP flakes on 90nm-SiO₂/Si substrate for $\lambda_i=633\text{nm}$, and the corresponding (b1,b3) $|c_{\text{eff}}|/|a_{\text{eff}}|$ and (b2,b4) Φ_{eff} for A_g^1 and A_g^2 modes with varied d_{BP} and d_{SiO_2} .

A_g^2 modes in each BP flake can be determined by fitting the corresponding ARPR intensity in Fig.1(f) and Fig.S4, as illustrated in Fig.2(d). The average $|c_{\text{int}}|/|a_{\text{int}}|$ and ϕ_{int} of the A_g^1 and A_g^2 modes are used to calculate the ARPR intensity profile for BP flakes with varied d_{BP} (pink curves in Fig.2(e)), showing good agreement with the experimental ones.

The above constant $|c_{\text{int}}|/|a_{\text{int}}|$ and ϕ_{int} imply that the anisotropic e-pht ($M_{e-\text{pht}}$) and e-phn ($M_{e-\text{phn}}$) coupling matrices are almost unchanged for BP flakes ($d_{\text{BP}} > 20\text{nm}$), which can be ascribed to the similar electronic band structure[9]. In addition, $|c_{\text{int}}|/|a_{\text{int}}|$ for A_g^1 and A_g^2 modes are both larger than 1, indicating a larger $M_{e-\text{pht}(s)} \cdot M_{e-\text{phn}} \cdot M_{e-\text{pht}(i)}$ along Z axis than that along X axis owing to the much larger light absorption along Z axis[9, 29]. The larger $|c_{\text{int}}|/|a_{\text{int}}|$ of A_g^2 (~ 1.6) than A_g^1 (~ 1.18) mode implies that the ratio of $M_{e-\text{phn}}$ between the Z and X axes for A_g^2 mode is ~ 1.4 times of that for A_g^1 mode. Furthermore, the nonzero ϕ_{int} in \mathbf{R}_{int} for both A_g^1 and A_g^2 modes are induced by the anisotropic dielectric function due to the linear dichroism in BP flakes.

With the above insights into the modulations from birefringence, linear dichroism, anisotropic interference effects, and anisotropic e-pht (e-phn) coupling[9, 18] in Raman scattering process of BP flakes, we aim to integrate all these effects to derive the formalism of effective elements in \mathbf{R} to directly predict their ARPR response. By comparing the Eq.4 with the Eq.1, we can get the formalism for \mathbf{R} as follows,

$$\frac{|c_{\text{eff}}|}{|a_{\text{eff}}|} = \left(\frac{|c_{\text{int}}|}{|a_{\text{int}}|} \right) \cdot \left(\frac{F_Z}{F_X} \right)$$

$$\Phi_{\text{eff}} = \arccos \left(\frac{\int_0^{d_{\text{BP}}} A_X A_Z \cos(\varphi_X - \varphi_Z + \phi_{\text{int}}) dy}{F_X F_Z} \right) \quad (5)$$

where $F_X = \sqrt{\int_0^{d_{\text{BP}}} A_X^2 dy}$ and $F_Z = \sqrt{\int_0^{d_{\text{BP}}} A_Z^2 dy}$ with A_X and A_Z the amplitudes of $F_{iX}(y)F_{sX}(y)$ and $F_{iZ}(y)F_{sZ}(y)$, respectively. φ_X and φ_Z are defined as the phases of $F_{iX}(y)F_{sX}(y)$ and $F_{iZ}(y)F_{sZ}(y)$, respectively.

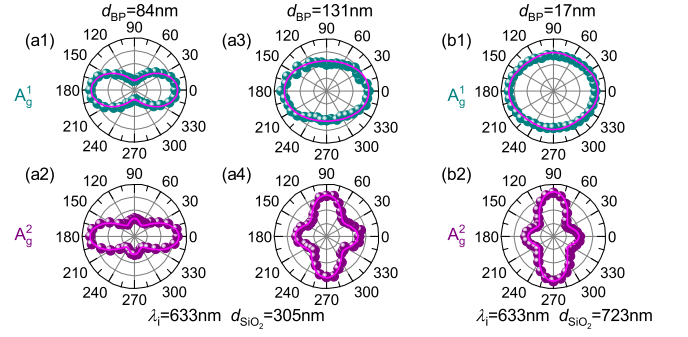


FIG. 4. Experimental (filled circles) and predicted (pink lines) ARPR intensity profiles for A_g^1 and A_g^2 modes of BP flakes with (a1,a2) $d_{\text{BP}}=84\text{nm}$ and (a3,a4) $d_{\text{BP}}=131\text{nm}$ on 305nm-SiO₂/Si substrate, and of (b) 17 nm BP flake on 723nm-SiO₂/Si substrate, where the predicted ones are calculated with $|c_{\text{eff}}|/|a_{\text{eff}}|$ and Φ_{eff} in Fig.S6(b).

With these analysis, we numerically calculated $|c_{\text{eff}}|/|a_{\text{eff}}|$ and Φ_{eff} for A_g^1 and A_g^2 modes in BP flakes on 90nm-SiO₂/Si with $\lambda_i=633\text{nm}$, as elucidated in Fig.3(a). Both $|c_{\text{eff}}|/|a_{\text{eff}}|$ and Φ_{eff} are sensitive to d_{BP} . With the derived \mathbf{R} with effective elements, one can predict the ARPR intensity for BP flakes. Good agreements between the predicted and experimental ARPR intensity for $\lambda_i=633\text{nm}$ are shown in Fig.S5. The periodic variations of $|c_{\text{eff}}|/|a_{\text{eff}}|$ and Φ_{eff} of BP flakes give rise to periodic changes of the ARPR intensity shape. It is clear that the complicated dependencies of $|c_{\text{eff}}|/|a_{\text{eff}}|$ and Φ_{eff} on d_{BP} is the main reason for the challenge in predicting ARPR intensity for BP flakes in previous studies[6–9, 12, 16]. Similar derivation for \mathbf{R} can be applied to other anisotropic ALM flakes to acquire a quantitative prediction of the ARPR response.

Owing to the evident optical interference effect for the BP/SiO₂/Si multilayer structure, $|c_{\text{eff}}|/|a_{\text{eff}}|$ and Φ_{eff} are also sensitive to d_{SiO_2} . We plot the dependencies of $|c_{\text{eff}}|/|a_{\text{eff}}|$ and Φ_{eff} on d_{SiO_2} and d_{BP} for A_g^1 and A_g^2 modes in Fig.3(b). The $|c_{\text{eff}}|/|a_{\text{eff}}|$ ratio of A_g^1 mode consistently remains smaller than that of the A_g^2 mode. Similar behaviors are found for the Φ_{eff} . With these predicted $|c_{\text{eff}}|/|a_{\text{eff}}|$ and Φ_{eff} , the ARPR intensities for BP flakes on SiO₂/Si substrates with different d_{SiO_2} are also predictable, as exemplified by the ARPR intensity of BP flakes with $d_{\text{BP}}=84\text{nm}$ and 131nm on 305nm-SiO₂/Si substrate in Fig.4(a). The predicted ARPR intensities well reproduce the measured ones.

In particular, similar to the case of \tilde{n}_X and \tilde{n}_Z , \mathbf{R}_{int} should also be sensitive to the number of layers of thin BP flakes. Thus, one can obtain the tensor elements ($|c_{\text{int}}|/|a_{\text{int}}|$ and ϕ_{int}) by fitting the ARPR intensities of specific BP flake on SiO₂/Si substrates with different d_{SiO_2} , whose \tilde{n}_X and \tilde{n}_Z are determined by reflectance measurements (Fig.2(c)). As exemplified by 17 nm BP flake, the fitted $|c_{\text{int}}|/|a_{\text{int}}|$ and ϕ_{int} are elucidated in Fig.S6, whose average values are indicated by the

dashed lines. Accordingly, the ARPR intensities for 17 nm BP flakes on other substrates can be quantitatively predicted by the Eqs.1 and 5, as illustrated in Fig.4(b) and Figs.S6(c,d). Once the preparation technique for stable few-layer BP flakes can be achieved, one can also quantitatively predict its ARPR intensity. This methodology can be extended to other few-layer ALM flakes, as demonstrated in Section VI, Fig.S7 and Fig.S8 with 4-layer T_d -WTe₂ flake under 633nm and 532nm excitations as examples. The good agreement between the predicted and experimental ARPR intensity profiles further confirms that one can quantitatively predict the ARPR intensity profiles of specific few-layer ALM flakes with experimentally-determined \mathbf{R}_{int} via analyzing ARPR intensity profiles of specific ALM flake deposited on SiO₂/Si substrates with varied d_{SiO_2} .

The above methodologies to acquire complex refractive indexes (\tilde{n}_X , \tilde{n}_Z) and \mathbf{R}_{int} elements ($|c_{\text{int}}|/|a_{\text{int}}|$ and ϕ_{int}) of A_g^1 and A_g^2 modes for BP flakes can be extended to other λ_i , e.g., 532nm (Fig.S9-10) and 488nm (Fig.S11-12). With these parameters, one can calculate the effective $|c_{\text{eff}}|/|a_{\text{eff}}|$ and Φ_{eff} in \mathbf{R} for BP flakes on SiO₂/Si substrate with varied d_{SiO_2} and d_{BP} for $\lambda_i=532\text{nm}$ (Fig.S13) and 488nm (Fig.S14), which can successfully reproduce the observed ARPR intensities of A_g^1 and A_g^2 modes for BP flakes without any additional fitting parameters (Fig.S15-16). This suggests the general validity of our proposed strategy to predict ARPR intensities of ALM flakes under varied λ_i excitations by the experimentally-determined \mathbf{R}_{int} elements.

In conclusion, Raman selection rule in BP flakes is influenced by birefringence, linear dichroism, optical interference effects of multilayer structures, and \mathbf{R}_{int} . We proposed strategies to delineate the intrinsic ($|c_{\text{int}}|/|a_{\text{int}}|$ and ϕ_{int}) and effective ($|c_{\text{eff}}|/|a_{\text{eff}}|$ and Φ_{eff}) Raman tensor elements for phonon modes of BP flakes, which can be applied to accurately predict the corresponding ARPR intensity profiles of BP flakes on various substrates. This research overcomes the challenge in predicting ARPR intensity in ALM flakes.

We acknowledge the support from the National Key Research and Development Program of China (Grant No. 2023YFA1407000), the Strategic Priority Research Program of CAS (Grant No. XDB0460000), National Natural Science Foundation of China (Grant Nos. 12322401, 12127807 and 12393832), CAS Key Research Program of Frontier Sciences (Grant No. ZDBS-LY-SLH004), Beijing Nova Program (Grant No. 20230484301), Youth Innovation Promotion Association, Chinese Academy of Sciences (No. 2023125) and CAS Project for Young Scientists in Basic Research (YSBR-026).

- [1] Loudon, R. The raman effect in crystals. *Adv. Phys.* **13**, 423–482 (1964).
- [2] Cardona, M. (ed.) *Light Scattering in Solids I*, vol. 8 (Springer-Verlag, Berlin, 1983).
- [3] Kranert, C., Sturm, C., Schmidt-Grund, R. & Grundmann, M. Raman tensor formalism for optically anisotropic crystals. *Phys. Rev. Lett.* **116**, 127401 (2016).
- [4] Kranert, C., Sturm, C., Schmidt-Grund, R. & Grundmann, M. Raman tensor elements of β -Ga₂O₃. *Sci. Rep.* **6**, 35964 (2016).
- [5] Lin, M.-L. *et al.* Understanding angle-resolved polarized raman scattering from black phosphorus at normal and oblique laser incidences. *Sci. Bull.* **65**, 1894–1900 (2020).
- [6] Ribeiro, H. B. *et al.* Unusual angular dependence of the Raman response in black phosphorus. *ACS Nano* **9**, 4270–4276 (2015).
- [7] Kim, J. *et al.* Anomalous polarization dependence of Raman scattering and crystallographic orientation of black phosphorus. *Nanoscale* **7**, 18708–18715 (2015).
- [8] Mao, N. *et al.* Birefringence-directed Raman selection rules in 2D black phosphorus crystals. *Small* **12**, 2627–2633 (2016).
- [9] Ling, X. *et al.* Anisotropic electron-photon and electron-phonon interactions in black phosphorus. *Nano Lett.* **16**, 2260–2267 (2016).
- [10] Phaneuf-L’Heureux, A.-L. *et al.* Polarization-resolved raman study of bulk-like and davydov-induced vibrational modes of exfoliated black phosphorus. *Nano Lett.* **16**, 7761–7767 (2016).
- [11] Zheng, W., Yan, J., Li, F. & Huang, F. Elucidation of “phase difference” in raman tensor formalism. *Photon. Res.* **6**, 709–712 (2018).
- [12] Choi, Y. *et al.* Complete determination of the crystallographic orientation of ReX₂ (X = S, Se) by polarized raman spectroscopy. *Nanoscale Horiz.* **5**, 308–315 (2020).
- [13] Zhu, Y. *et al.* Raman tensor of layered black phosphorus. *Photonix* **1**, 17 (2020).
- [14] Pimenta, M. A., Resende, G. C., Ribeiro, H. B. & Carvalho, B. R. Polarized raman spectroscopy in low-symmetry 2d materials: angle-resolved experiments and complex number tensor elements. *Phys. Chem. Chem. Phys.* **23**, 27103–27123 (2021).
- [15] Zou, B. *et al.* Unambiguous determination of crystal orientation in black phosphorus by angle-resolved polarized raman spectroscopy. *Nanoscale Horiz.* **6**, 809–818 (2021).
- [16] Huang, S. *et al.* In-plane optical anisotropy of layered gallium telluride. *ACS Nano* **10**, 8964–8972 (2016).
- [17] Wu, J., Mao, N., Xie, L., Xu, H. & Zhang, J. Identifying the crystalline orientation of black phosphorus using angle-resolved polarized Raman spectroscopy. *Angew. Chem. Int. Ed.* **54**, 2366–2369 (2015).
- [18] Mao, N. *et al.* Direct observation of symmetry-dependent electron-phonon coupling in black phosphorus. *J. Am. Chem. Soc.* **141**, 18994–19001 (2019).
- [19] Strach, T., Brunen, J., Lederle, B., Zegenhagen, J. & Cardona, M. Determination of the phase difference between the Raman tensor elements of the A_{1g} -like phonons in SmBa₂Cu₃O_{7- δ} . *Phys. Rev. B* **57**, 1292–1297 (1998).
- [20] Li, X.-L. *et al.* Layer number identification of intrinsic

- and defective multilayer graphenes by the Raman mode intensity from substrate. *Nanoscale* **7**, 8135–8141 (2015).
- [21] Ribeiro-Soares, J. *et al.* Group theory analysis of phonons in two-dimensional transition metal dichalcogenides. *Phys. Rev. B* **90**, 115438 (2014).
- [22] Wu, J.-B., Lin, M.-L., Cong, X., Liu, H.-N. & Tan, P.-H. Raman spectroscopy of graphene-based materials and its applications in related devices. *Chem. Soc. Rev.* **47**, 1822–1873 (2018).
- [23] Lin, M.-L. *et al.* Cross-dimensional electron-phonon coupling in van der Waals heterostructures. *Nat. Commun.* **10**, 2419 (2019).
- [24] Dawson, P. Polarisation measurements in Raman spectroscopy. *Spectrochim. Acta Part A* **28**, 715–723 (1972).
- [25] Rulmont, A. & Flamme, J. Birefringence effect in the Raman spectrum of a crystal which is not cut parallel to the principal axes-I. *Spectrochim. Acta Part A* **35**, 629–633 (1979).
- [26] Rulmont, A., Flamme, J., Pottier, M. & Wanklyn, B. Birefringence effect in the Raman spectrum of a crystal which is not cut parallel to the principal axes-II. application to a single crystal of LaBO_3 . *Spectrochim. Acta Part A* **35**, 635 – 639 (1979).
- [27] Alonso-Gutiérrez, P., Sanjuán, M. L. & Morón, M. C. Raman selection rules in uniaxial media: The nonpolar modes of MnGa_2Se_4 . *Phys. Rev. B* **71**, 085205 (2005).
- [28] Zhang, H. *et al.* Cavity-enhanced linear dichroism in a van der waals antiferromagnet. *Nat. Photon.* **16**, 311–317 (2022).
- [29] Qiao, J., Kong, X., Hu, Z.-X., Yang, F. & Ji, W. High-mobility transport anisotropy and linear dichroism in few-layer black phosphorus. *Nat. Commun.* **5**, 4475 (2014).
- [30] Marianne, K. *et al.* Access and in situ growth of phosphorene-precursor black phosphorus. *J. Cryst. Growth* **405**, 6–10 (2014).
- [31] Castellanos-Gomez, A. *et al.* Deterministic transfer of two-dimensional materials by all-dry viscoelastic stamping. *2D Materials* **1**, 011002 (2014).
- [32] Kim, M. *et al.* Determination of the thickness and orientation of few-layer tungsten ditelluride using polarized raman spectroscopy. *2D Mater.* **3**, 034004 (2016).
- [33] Lee, J. *et al.* Single- and few-layer WTe_2 and their suspended nanostructures: Raman signatures and nanomechanical resonances. *Nanoscale* **8**, 7854–7860 (2016).
- [34] Luo, Z. *et al.* Anisotropic in-plane thermal conductivity observed in few-layer black phosphorus. *Nat. Commun.* **6**, 8572 (2015).
- [35] Born, M. & Wolf, E. *Principles of Optics: Electromagnetic Theory of Propagation, Interference and Diffraction of Light* (Cambridge University Press, Cambridge, 1999), 7 edn.
- [36] Wang, Y. Y., Ni, Z. H., Shen, Z. X., Wang, H. M. & Wu, Y. H. Interference enhancement of Raman signal of graphene. *Appl. Phys. Lett.* **92**, 043121 (2008).
- [37] Yoon, D. *et al.* Interference effect on raman spectrum of graphene on SiO_2/Si . *Phys. Rev. B* **80**, 125422 (2009).
- [38] Kennedy, J. & Eberhart, R. Particle swarm optimization. In *Proceedings of ICNN'95 - International Conference on Neural Networks*, vol. 4, 1942–1948 vol.4 (1995).
- [39] Hoffmann, J. *Linear Regression Models: Applications in R* (Chapman and Hall/CRC., New York, 2021), 1 edn.
- [40] Kong, W.-D. *et al.* Raman scattering investigation of large positive magnetoresistance material WTe_2 . *Appl. Phys. Lett.* **106**, 081906 (2015).
- [41] Song, Q. *et al.* The in-plane anisotropy of WTe_2 investigated by angle-dependent and polarized raman spectroscopy. *Sci. Rep.* **6**, 29254 (2016).